EUROPEAN SYNCHROTRON RADIATION FACILITY

INSTALLATION EUROPEENNE DE RAYONNEMENT SYNCHROTRON

ESRF

Experiment Report Form

The double page inside this form is to be filled in by all users or groups of users who have had access to beam time for measurements at the ESRF.

Once completed, the report should be submitted electronically to the User Office via the User Portal:

https://wwws.esrf.fr/misapps/SMISWebClient/protected/welcome.do

Reports supporting requests for additional beam time

Reports can be submitted independently of new proposals – it is necessary simply to indicate the number of the report(s) supporting a new proposal on the proposal form.

The Review Committees reserve the right to reject new proposals from groups who have not reported on the use of beam time allocated previously.

Reports on experiments relating to long term projects

Proposers awarded beam time for a long term project are required to submit an interim report at the end of each year, irrespective of the number of shifts of beam time they have used.

Published papers

All users must give proper credit to ESRF staff members and proper mention to ESRF facilities which were essential for the results described in any ensuing publication. Further, they are obliged to send to the Joint ESRF/ ILL library the complete reference and the abstract of all papers appearing in print, and resulting from the use of the ESRF.

Should you wish to make more general comments on the experiment, please note them on the User Evaluation Form, and send both the Report and the Evaluation Form to the User Office.

Deadlines for submission of Experimental Reports

- 1st March for experiments carried out up until June of the previous year;
- 1st September for experiments carried out up until January of the same year.

Instructions for preparing your Report

- fill in a separate form for each project or series of measurements.
- type your report, in English.
- include the reference number of the proposal to which the report refers.
- make sure that the text, tables and figures fit into the space available.
- if your work is published or is in press, you may prefer to paste in the abstract, and add full reference details. If the abstract is in a language other than English, please include an English translation.

ESRF	**Experiment title:** ***"on chip" microreactor: suited tool for X-ray analysis within high pressure media***	**Experiment number**:
Beamline:	**Date of experiment**: from: 24/06/2013 to: 28/06/2013	**Date of report**: 02/03/2015
Shifts:	**Local contact(s)**: Pawel Kwasniewski	*Received at ESRF:*

Names and affiliations of applicants (* indicates experimentalists):

Thomas Beuvier, Alain Gibaud, Elvia Chavez, IMMM, Université du Maine

Brice Calvignac, MINT, Université d'Angers

Report:

A successful implementation of *in situ* X-ray scattering analysis of synthetized particle materials in silicon/glass microreactors is reported. Calcium carbonate ($CaCO_3$) as a model material was precipitated inside the microchannels through the counter-injection of two aqueous solutions, containing carbonate ions and calcium ions, respectively. The synthesized calcite particles were analyzed *in situ* in aqueous media by combining Small Angle X-ray Scattering (SAXS) and Wide Angle X-ray Scattering (WAXS) techniques at the ESRF ID02 beam line. At high wavevector transfer, WAXS patterns clearly exhibit different scattering features: broad scattering signals originating from the solvent and the glass lid of the chip, and narrow diffraction peaks coming from $CaCO_3$ particles precipitated rapidly inside the microchannel. At low wavevector transfer, SAXS reveals the rhombohedral morphology of the calcite particles together with their micrometer size without any strong background, neither from the chip nor from the water. This study demonstrates that silicon/glass chips are potentially powerful tools for *in situ* SAXS/WAXS analysis and are promising for studying the structure and morphology of materials in non-conventional conditions like geological materials under high pressure and high temperature.

This work will be published in Lab on a chip with the title :
"Implementation of in situ SAXS/WAXS characterization into silicon/glass microreactors".

1. Introduction

Optically transparent integrated microfluidic devices are widely used in biology,[1] chemistry,[2] and material science[3] mainly because optical *in situ* characterization, such as microscopic observations,[4] dynamic light scattering,[5] or light spectroscopy (UV-vis,[6] Raman,[7] photoluminescence[8]), can be

easily performed inside microchannels. Additionally, thanks to the advancement of synchrotron sources, Small-Angle and Wide-Angle X-ray scattering (SAXS/WAXS) studies utilizing microfluidic devices are more and more used, notably to characterize the morphology and the structure of proteins,[9] nucleic acids,[10] biomacromolecules,[11,12] or inorganic nanoparticles.[13]

Amongst the transparent microfluidics systems, most of them are fabricated from silicone elastomers (such as polydimethylsiloxane PDMS). As silicone elastomers are permeable to water vapor, they are sometimes replaced by rigid thermoplastics including cyclic olefin homopolymer (COP), polystyrene (PS), or poly-methyl methacrylate (PMMA). These polymers have high transparency and low fluorescence over a wide visible spectral range. These microreactors often make excellent prototypes but they have limited operating pressure and temperature ranges, as well as poor chemical compatibility with most of the organic solvents.

Alternative experimental setups can overcome some of the above difficulties, in particular under high pressure and temperature, by considering glass or sapphire capillaries.[14,15,16] Their high compatibility with many organic solvents and their good resistance to aggressive chemicals extend the scope of fluids that can be used. However, glass tubings suffer from low design flexibility and exhibit poor heat transfers. Additionally, it is extremely difficult to design fancy mixing devices in a glass capillary.

The development of on-chip silicon-glass microsystems has addressed the optimization of both the experimental approaches towards the use of a large panel of fluids and solvents, as well as the extent of the operating conditions of these micro systems at high temperature and high pressure.[3,17,18] The use of top borosilicate glass wafers anodically bonded to silicon also provides the optical access.[19] Moreover, advanced microfabrication techniques can be easily used from silicon and glass wafers, providing for a wide range of designs, from two dimensional layouts extruded in the third dimension to fully three dimensional structures. This design flexibility allows for the precise manipulation of hydrodynamics and has greatly facilitated the *in situ* observation of chemical reactions with the possibility to study minute quantities of fluids while ensuring high temperature, high pressure capabilities to enlarge the field of applications, such as phase diagram investigations,[20] fuel conversion,[21] nanomaterials synthesis[22,23] or chemistry.[24,25] However, literature concerning the use of silicon/glass chips with X-ray scattering techniques is rather scarce, especially in the case of SAXS/WAXS experiments. The requirement of a small beam size (in the micron range) and high intensity are among the main limiting factors, while the optimum experimental conditions can be certainly provided at synchrotron beam lines.

X-ray scattering experiments coupled to silicon-glass microreactors for studying the *in situ* formation of crystallized particles is thus the main concern of this paper. Although amorphous glasses cannot be considered as being the perfect materials for X-ray scattering at wide angle,[26] they offer here the optical access to check the results of the SAXS and WAXS analyses concerning the particle structure and morphology. Indeed, this double diagnostic optical/X-ray appears as the essential preliminary

mean to anticipate the feasibility of X-ray scattering on future *blind* silicon-silicon systems. The ID02 beam line at ESRF (Grenoble - France) allows for simultaneous SAXS and WAXS measurements with a good spatial resolution.

To examine the feasibility of using silicon/glass microreactors, we have chosen the calcium carbonate ($CaCO_3$) as a model material to investigate the structure and the morphology of the crystallized microparticles. Calcium carbonate is interesting because it is abundant in biominerals or geological formations and largely used in numerous domains due to its wide use as an additive supporting product in paints, plastics or paper or as smart microcarriers in biomedical applications. Among the $CaCO_3$ polymorphs, vaterite exhibits generally a spherical morphology.[27,28] Aragonite looks like needles and is well known to precipitate only at temperature above around 40°C.[29] Finally, calcite has a trigonal crystal system with a $R\bar{3}c$ space group and exhibit various polygonal morphologies. The majority of the calcite crystals adopt a randomly oriented rhombohedral form with angles between the faces close to $\alpha = 76°$.[30]

Additionally, $CaCO_3$ exhibits low solubility. At 25°C, the solubility constants are $K_{sp} = 10^{-6.4}$, $10^{-7.9}$, $10^{-8.3}$ and $10^{-8.5}$ for the amorphous calcium carbonate (ACC),[31] vaterite, aragonite and calcite,[32] respectively. $CaCO_3$ can thus precipitate easily by mixing two aqueous solutions of very low concentrations, one containing the carbonate ions CO_3^{2-} and the other the calcium ions Ca^{2+}, as previously reported.[33,34,35] Without any additive reagent, calcite and vaterite are mostly obtained in synthesis performed at ambient temperature, whereas aragonite appears at higher temperatures (T > 40°C).[34]

The following sections briefly describe the silicon/glass microreactor used in this study, before showing and discussing the SAXS and WAXS results obtained during the counter-injection of the two aqueous solutions to form calcium carbonate in the resulting continuous mixing flow. It is worth noticing that the various experimental parameters (concentration, temperature, pH, mixing efficiency, residence time, etc.) involved during the precipitation of the different polymorphs of $CaCO_3$ have already been investigated in the literature.[29,30,31,32,33,34,35] Therefore the present concern is only focused on the intrinsic capabilities of the *in situ* SAXS and WAXS analyses to distinguish the structure and morphology of the particles inside a microchannel of a silicon-glass microreactor, not on the inherent challenges of using microfluidic devices to control the nucleation and growth of these crystals.

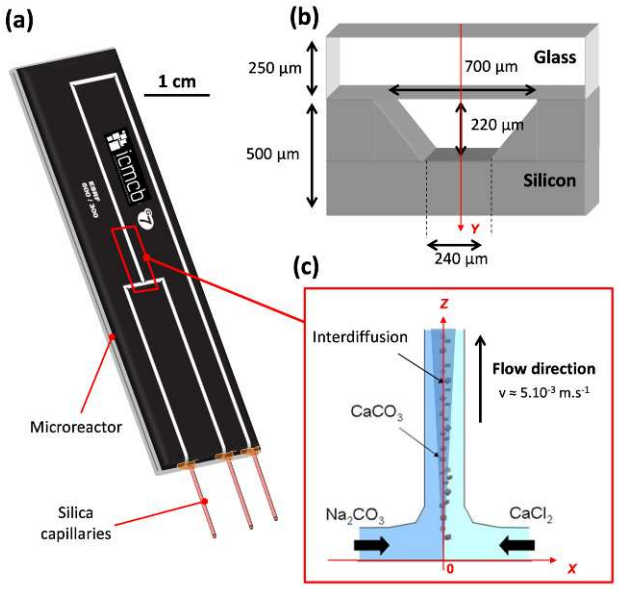

Fig. 1 (a) General view of the silicon/Pyrex microreactor. (b) Typical sizes of the channel cross-section of the microreactor. (c) Schematic illustration of the T-junction part (red insert in (a)) showing the counter flow injection of the two solutions in the horizontal inlet channels and their mixing flow in the vertical main channel where the calcium carbonate precipitates in the interdiffusion zone. The *x*, *y* and *z* are defined in (b) and (c).

2. Experimental approach and techniques

2.1 Microfluidic device fabrication

The silicon-glass microreactors were fabricated [3,18] through the patterning of the commercial silicon wafers (photolithography + wet etching), which were subsequently anodically bonded to commercial Pyrex 7740 wafers to provide the optical access to the patterned channels from the corresponding microreactor glass part. Our present design consists of two inlet microchannels merging at a T-junction feeding a larger main channel of interest (Figure 1-a). The dimensions of the chip were *8* cm by *2* cm for a total thickness of *750* µm including *500* µm of silicon and a *250* µm Pyrex lid. The microchannels (*220* µm deep) were obtained by chemical etching of silicon, leading to a trapezoidal cross section exhibiting a width ranging from *240* µm at the bottom to *700* µm at the top for the main channel (Figure 1-b). Reagents were introduced into two 10 mL syringes and co-injected using a syringe pump (Model 101, KD Scientific) through silica capillaries epoxy-glued to the two inlet channels. The microreactors were mounted vertically along the main channel whose axis corresponds to the *z*-axis in our experimental orthonormal basis (see Figure 1-c). In the following, $z = 0$ denotes the bottom part of the inlet and main channel, while the *x* and *y* axes refer to the transverse and colinear directions of the X-ray beam, respectively (Figures 1-c and 1-b).

2.2 Precipitation of $CaCO_3$ inside the channel

Two glass syringes, containing aqueous solutions of calcium chloride ($[CaCl_2]$ = 0.010 M) and sodium carbonate ($[Na_2CO_3]$ = 0.010 M), respectively, were connected to the silica capillaries. The two fluids were injected at constant flow rates into the microreactor at ambient temperature and pressure. In this study, the selected flow rate was 20 µL.min^{-1}, leading to a flow velocity in the main channel of 5.2 mm.s^{-1}. The precipitation of $CaCO_3$ crystals occurs as soon as the product of the concentrations of Ca^{2+} and CO_3^{2-} becomes larger than the solubility constant of the $CaCO_3$ phase. Choosing $[Ca^{2+}] = [CO_3^{2-}] = 0.010$ M as a typical reagent concentration leads to $[Ca^{2+}].[CO_3^{2-}] = 10^{-4}$ M², which is far higher than the solubility constants K_{sp} of $CaCO_3$. The two aqueous solutions were flown in opposite directions inside the inlet channels and mixed at the T-junction. Given that the flow regime was laminar (Re ~ 2.5 in our conditions), each of the two solutions filled half of the microchannel cross-section and the mixing - driven by diffusion - occurred at the interface, leading to the formation of $CaCO_3$ particles within the interdiffusion zone (see schematic Figure 1-c).

2.3 SAXS and WAXS analysis

SAXS and WAXS measurements were collected at the ID02 beam line (ERSF) at energy of 12.490 keV with a beam size of 50 µm x 50 µm cross-section. The SAXS and WAXS images were recorded using 2D image-intensified CCD camera detectors. The sample-to-detector distances were set to 10 cm and 10 m for the WAXS and SAXS detectors, respectively. The magnitudes of the wavevector transfer $\bar{q}$ were ranges from 10 nm^{-1} to 45 nm^{-1} for WAXS and from 0.008 nm^{-1} to 0.2 nm^{-1} for SAXS. All measurements were dark subtracted. The very high flux used at ID02 combined to the high sensitivity of each CCD detector allowed for fast acquisition of less than 200 ms per image.

3. Results and discussions

3.1 X-ray mapping image of the microreactor

The use of silicon-glass microreactors for *in situ* X-ray analysis can be affected by the absorption and the scattering of the microsystems itself. These two parameters are of paramount importance to discriminate the signals coming from the flowing fluids from the ones from the microreactor. We first started with the mapping image of the microchannel using the difference of the X-ray beam absorption when crossing or not the channel. The absorption depends mainly on the photoelectric absorption of photons by the material, thereby decreasing the intensity of both the transmitted and the diffracted X-rays. Considering a narrow beam (50 µm x 50 µm cross-section) of mono energetic photons at a wavelength λ_0, with an incident intensity I_0, penetrating a layer of thickness y, and finally emerging with an intensity I, the transmission T can be defined as :[36]

$$T(\lambda_0) = I(\lambda_0) / I_0(\lambda_0) = \exp(-\mu.\rho.y) = \exp(-y / \lambda_a) \quad (1)$$

with μ being the photoabsorption cross section, ρ the layer density and λ_a the attenuation length. For the photon energy of 12.490 keV (used in this work), $\lambda_a^{Si} \sim 257.4$ µm for silicon and $\lambda_a^{glass} \sim 487.9$ µm for glass.[36] Due to the large penetration depth of X-rays in these materials, relatively thick microsystems (in the order of a few hundreds of micrometers) could be used.

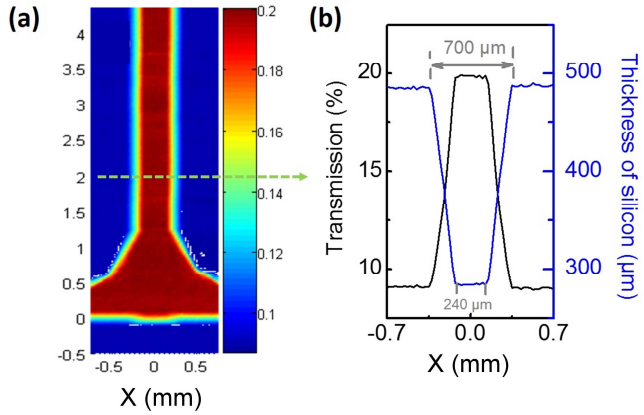

Fig. 2(a) X-ray transmission imaging of the T-junction part of the empty chip. (b) Scanning profile of the transmission T (%) (left axis - black curve) and related silicon thickness in µm (right axis - blue curve) along the yellow dotted line of (a) (see text for detail).

To localize the T-junction inside the chip, the channel was imaged using scanning X-rays in transmission along the *y* axis (Figure 2-a). Such a X-ray radiography of the microreactor has the advantage to be more quantitative than optical microscopy in transmission. In particular the X-ray imaging provides access to the depth of the channel. Indeed, for a silicon/glass bilayer system, the transmission is defined as:

$$T(\lambda_0) = \exp(-y_{Si} / \lambda_a^{Si}).\exp(-y_{glass} / \lambda_a^{glass}) \quad (2)$$

where λ_a^{Si} and λ_a^{glass} are the attenuation coefficients of silicon and glass respectively, and y_{Si} and y_{glass} their respective thicknesses. With $\lambda_a^{Si} = 257.4$ µm and $\lambda_a^{glass} = 487.9$ µm, the calculated transmission is $T \sim 8.6\%$ outside the channel for which $y_{Si} = 500$ µm and $y_{glass} = 250$ µm and $T \sim 20.1\%$ in the middle of the channel where $y_{Si} = 280$ µm. These values are close to those obtained from Figures 2-a and 2-b where the sample was translated vertically and horizontally every *25* µm to scan a mapping image of the T-junction. At each position, the acquisition time was *200* µs. As a typical result, the transmission profile at $z = 2$ mm is shown as a black curve in Figure 2-b (left axis). From the

transmission profile, it is then possible to reconstruct its depth profile, as shown by the blue curve (right axis). Nevertheless, this reconstruction does not give the true profile of the channel as the measured profile is the convolution of the direct beam profile with the true profile of the channel. In this case the beam cross-section size was not small enough to approximate the direct beam to a delta function. The depth profile of the channel is thus smeared out by the instrumental resolution.

3.2 SAXS and WAXS experiments using Si/glass microreactors

In addition to the X-ray transmission mapping, the capabilities of silicon/glass microsystems for X-ray analysis were checked by performing two types of *in situ* scattering experiments: SAXS at small wavevector transfer values $q < 10$ nm^{-1} and WAXS for $q > 10$ nm^{-1}. We now address the interest of silicon/glass microreactors for *in situ* WAXS and SAXS analysis considering, in the following study, the particular position $x = 0$, $z = 1$ mm for the axis of the illuminated channel volume by the X-ray beam of 50 µm x 50 µm cross-section. The related results obtained from the WAXS and SAXS signals at several positions along the channel *z*-axis are discussed in S1.

SAXS signals originate from electron density heterogeneities at the mesoscale. It is indeed straightforward to show that homogenous materials, such as glass and silicon, do not produce any signal in the SAXS region, except at very small *q*, yielding only a low background signal. Note that the channel being etched, it is very likely that the inner surface of the channel is rough at the mesoscale so that even though silicon is homogeneous in nature it can yield a weak signal in SAXS experiments. Such a signal is however clearly position-dependent of the incident X-ray beam.

In the WAXS region, silicon wafers that are almost perfect single crystals with a cubic symmetry can only scatter when they are oriented in such a way that the Bragg law of reflection is satisfied. On the contrary glass exhibits a strong diffuse ring at $q \sim 15$ nm^{-1} corresponding to a *d*-spacing of *0.43* nm in the Bragg's law, related to its amorphous glassy state.[26]

In scattering experiments carried out in microfluidic devices, the measured signal is always the sum of the scattering by the investigated material particles to which are added the contributions of the solvent sample and the microfluidic device components. It is therefore mandatory to measure the WAXS and SAXS background signals at fixed *z*-position, of the empty chip in a first step (background due to the chip components), and then the chip filled with pure water in a second step (background due to the chip component + water mimicking the solvent sample). Subsequently, the 2 aqueous solutions (Na_2CO_3 0.010 M and $CaCl_2$ 0.010 M) are co-injected into the microreactor and X-ray scattering analysis can be carried out at selected *z*-positions, $x = 0$ and different working times, thus subtracting the corresponding chip + water background signal. Finally, optical microscopy observations of the microreactor are made after stopping the aqueous solutions flows and drying the

channels (typically 2 hours after the starting time of the aqueous solution injections at constant flow rate). The size of the $CaCO_3$ particles attached to the main channel can be then optically controlled. We now highlight the results measured *in situ* by WAXS before commenting the ones achieved by SAXS, using the *20* µL.min^{-1} constant flow rate. As mentioned above, all the following sections deal with the single *x = 0, z = 1* mm X-ray beam position, while S1 is focussed on the supplementary results at several positions along the *z*-axis. In addition we note that the *in situ* SAXS analysis was performed simultaneously to the WAXS analysis. However, in the present study, we failed to monitor the early stages of the calcite formation through the initial precipitates of amorphous calcium carbonate (ACC). We recall that the channel was filled with water at the very beginning of the aqueous solution injection and, as soon as the two solutions are mixed, a drastic change occurred in the scattering signal. However, it was always difficult to identify the precise moment at which the particles of interest are present in the illuminated volume since it was not possible to control either the initial number of ACC nanoparticles or the growing process of the calcite particles in the inter-diffusion zone. The selected SAXS and WAXS images were thus recorded only after a finite delay – typically ~ 1 minute – from the injection starting time of the reagents solutions.

3.2.1 WAXS - access to the particle structure

A typical example of the two-dimensional WAXS image is given in Figure 3-a, leading to the intensity profile of the azimuthal averaging plotted in Figure 3-b (grey curve). Similarly, the WAXS images of the empty chip and the chip filled with water lead to the intensity profiles plotted in black and blue curves, respectively, in Figure 3-b. The subtraction of the scattered intensities coming from the [particle+solvent+microsystem], the [microsystem+water] and the microsystem itself provides the pure scattered intensity signals of the microdevice, the water and the $CaCO_3$ crystallites (black, blue and red curves, respectively, in Figure 3-c). The observations of several isolated diffraction spots (marked by circles and indexed in Figure 3-a) are then clearly due to the presence of individual, oriented calcite microcrystals. These peaks are very narrow in width, showing that these particles are in the order of a few micrometers in size. The absence of rings in WAXS images confirms that no vaterite was formed since this variety is composed of randomly agglomerated nanocrystallites.[27] From Figure 3-b, it is very clear that the measured signal is dominated by both the two broad peaks (blue curve in Figure 3-c) of the *220* µm thick channel water, and also more significantly by the intense signal (black curve in Figure 3-c) coming from the *250* µm thick glass lid of the microfluidic system, the large width originating from the amorphous state of glass.[26] The high intensity comes from the high electron density of the glass (ρ_{glass} = *713* e$^-$.nm^{-3} assuming ρ = *2.2* g.cm^{-3}) compared to the one of water (ρ_{H2O} = *324* e$^-$.nm^{-3} assuming ρ = *1.0* g.cm^{-3}). The intensity of the Bragg peaks (red curve in Figure 3-c) of the microparticles of calcite differs from what could be expected from

randomly orientated calcite powder (purple line in Figure 3-b). In our case, we observed strong preferred orientations of the calcite crystallites leading, for example to different intensities distributions due to other orientations.

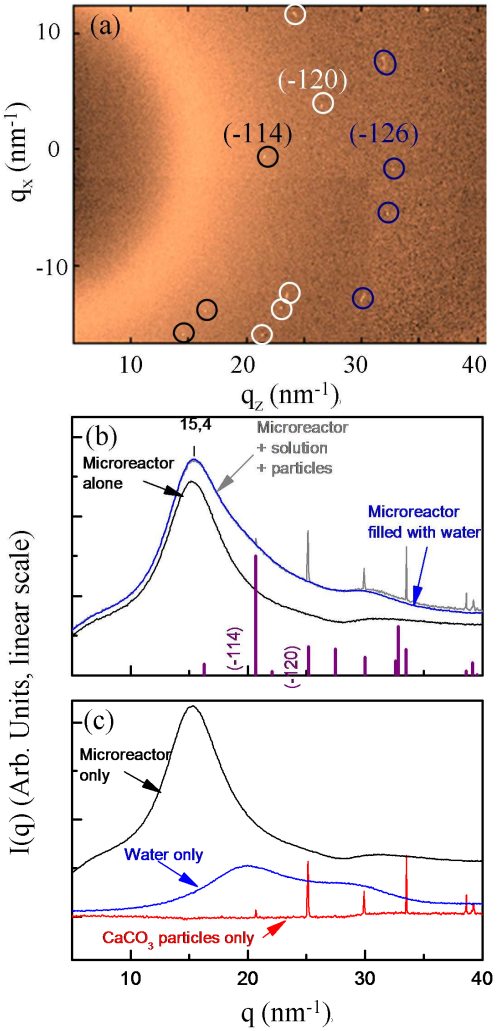

Fig. 3 (a) Example of an in situ WAXS image taken at x = 0 and z = 1 mm from the channel entrance and just after starting the injection of the 2 aqueous solutions (10 mM reagent). Indexed black, white, and blue circles: diffraction spots of oriented microcrystals [(-114) (black), (-120) or (110) (white), and (-126), (116) or (2-16) (blue)] of calcite. (b) Profile after azimuthal averaging of the (chip+solutions+particles) (grey), the chip+water (blue), and the chip alone (black) two-dimensional WAXS images. (c) Scattering from chip (black), water (blue) and $CaCO_3$ particles (red). The purples lines on the bottom axis of (c) are Bragg peaks of powder of calcite (see text for details).

3.2.2 SAXS - access to the particle morphology

The SAXS image shown in Figure 4-a was taken at the same place and the same time as the WAXS image of Figure 3-a. The observation of several streaks, such as the ones denoted s_1, s_2 and s_3 as typical examples in the figure, are attributed to the X-ray interaction with some individual, oriented microcrystals of calcite that were precipitated on the microreactors walls. These streaks are known as Crystal Truncation Rods (CTR) of each calcite single crystal. They originate from oriented facets delimiting rhombohedral calcite crystals of finite size.

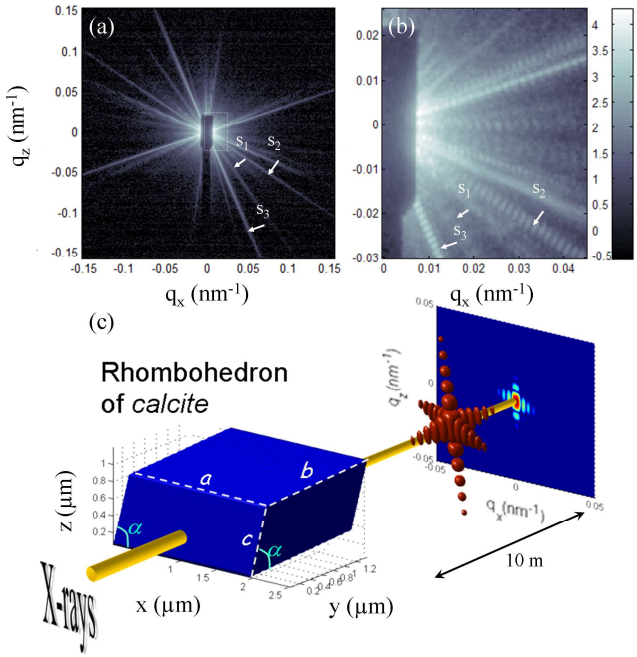

Fig. 4 (a) Example of an in situ SAXS image taken in similar conditions to Fig. 3. s1, s2 and s3): crystal truncation rods of oriented microcrystals of calcite. The observation of several streaks (denoted s1, s2 and s3) are attributed to the presence of individual, oriented microcrystals of calcite that were precipitated on the microreactors walls. These streaks are known as crystal truncation rods. (b) Zoom of the inserted tireted part of the SAXS image (a) to reveal the streak periodicity due to to the micrometer size of the calcite crystals. (c) Scheme (not to scale) showing the rhomboedron with edge of size a along the *x* axis and its related scattered intensity in the (q_x, q_z) plane. In red is shown the scattered intensity of the rhomboedron of calcite in a 3 dimensional view with an isocontour equal to $I_{max}/400$. I_{max} is the intensity at the center of the plane ($q_x = 0$ and $q_z = 0$). The dimensions of the rhomboedron is $a = 2$ µm (along x), $b = 1.5$ µm and $c = 1$ µm (in the xz-plane).

Indeed, a zoom (Figure 4-b) reveals that these streaks exhibit a pattern of fringes (the so-called Kiessig fringes) due to the micrometer size of these calcite crystals. The fringe periodicity Δq is inversely proportional to the distance size $\Lambda = 2\pi/\Delta q$ from two crystal facets being normal to the chosen crystal direction. In agreement with this formula, we can deduce that the periodicities of the

selected streaks s_1, s_2 and s_3 in Figures 4-a and 4-b correspond to calcite particles of typical sizes $\Lambda_1 = 1.9\,\mu m$, $\Lambda_2 = 3.7\,\mu m$ αvδ $\Lambda_3 = 4.3\,\mu m$, respectively.

The above observations can be understood from the expected rhombohedral structure of the calcite. Indeed, the scattering intensity of a single rhombohedron can be generally expressed as:

$$I(\vec{q}) = (\rho_0 - \rho_{sol})^2 . V^2 . \mathrm{sinc}^2\left(\frac{a.q_1}{2}\right) . \mathrm{sinc}^2\left(\frac{b.q_2}{2}\right) . \mathrm{sinc}^2\left(\frac{c.q_3}{2}\right) \quad (3)$$

a, *b*, *c* are the edge dimensions, $V = a.b.c.\sin^3(\alpha)$ is the rhombohedron volume with α the characteristic angle between the edges. ρ_0 is the electron density of the calcite rhombohedron and ρ_{sol} is the electron density of the solvent. By orienting the rhombohedron such as shown in Figure 4-c, i.e. the edge of size *a* is along the *x*-axis and the edge of size *c* is in the *xz*-plane, we can demonstrate that:

$$q_1 = q_x$$

$$q_2 = q_x \cos\alpha + q_y \frac{\sqrt{\sin^2\alpha - 2\cos^2\alpha + 2\cos^3\alpha}}{\sin\alpha} + q_z \frac{\cos\alpha - \cos^2\alpha}{\sin\alpha}$$

$$q_3 = q_x \cos\alpha + q_z \sin\alpha$$

where q_x, q_y, q_z, are the components of the wavevector tranfer $\vec{q}$ along the *x*-, *y*- and *z*-axis respectively.

It can be seen that the intensity at q_y = 0, *i.e.*, in the plane of the detector, couples q_x and q_z components as the different facets of the rhombohedron are not perpendicular to each other. Note also that we assume here that one of the facets lies parallel to the bottom of the channel of the microsystem. This assumption is likely to be incorrect as the channel surface is rough. Nevertheless, the shape of the Crystal Truncation Rods and the periodicity of the Kiessig Fringes obtained in the simulation results shown in Figure 4-c, reproduce fairly well the experimental observations assuming a rhombohedron with edges of size *a* = 2.0 µm (along *x*), *b* = 1.5 µm and *c* = 1.0 µm, with α = 76°.

In addition, simulations shown in S6 illustrate the importance of the orientation of the rhombohedron to change the scattered intensity.

Finally, these typical particle sizes are in good agreement with those obtained from optical microscopic observations after mixing the aqueous solutions ([$CaCl_2$] = 0.010 M and [Na_2CO_3] = 0.010 M) for ~ 1h at a flow rate of 20 µL.min^{-1} and after drying the channel for 1h at ambient temperature. Indeed, in Figure 5-a and 5-b, the microscopic images were focused either on the silicon side or on the glass side of the channel. For most of the particles of $CaCO_3$, the sizes are clearly below 10 µm, particularly when they are in contact with silicon. It is thus of great interest to assert optically that the sizes determined above from the periodicity of the streaks on the SAXS images are similar to the sizes of the remaining particles visible on the microscopic images of the dried microreactor, although the optical resolution is limited. This final optical control well confirms that

the presence of micrometric rhombohedra of calcite have been easily detected by SAXS as soon as there are precipitated and attached to the walls inside the microchannel.

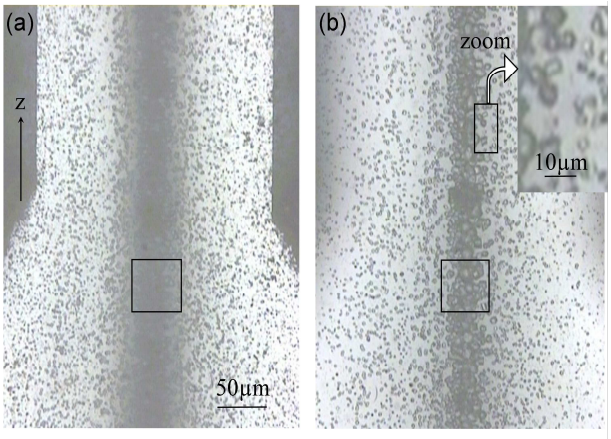

Fig. 5 Optical images obtained after mixing the aqueous solutions ([$CaCl_2$] = 0.010 M and [Na_2CO_3] = 0.010 M) for around 1h at a flow rate of 20µL.min^{-1} and after drying the chip for 1h at ambient temperature (a) focused at the silicon side of the channel, (b) focused at the glass side of the channel. The black squares show the position and the dimension of the X-ray beam where the SAXS and the WAXS analysis were done at the beginning of the crystallization process.

4. Conclusions and outlook

Silicon/glass microreactors have proven to be suitable devices for *in situ* X-ray scattered studies. By co-injecting two aqueous solutions in a T-junction, containing Ca^{2+} ions and CO_3^{2-} ions, respectively, we clearly highlight the formation of rhombohedra of calcite inside the microchannel. The shape of the formed particles and their micrometric size were revealed by SAXS and the calcite crystallographic structure was confirmed by WAXS. A control *a posteriori* of the morphology of the particles was here possible due to the optically transparent glass lid. The design of a blind silicon/silicon microreactor is now in progress: (i) to avoid the large diffusion of the glass lid in the WAXS region and (ii) to open avenues towards the X-ray studies of material behaviors in non-conventional, high-pressure, high-temperature media on chips, such as, for example, the ones providing (processing) hydrothermal and solvothermal syntheses, or the ones mimicking the geological aquifer formations during the CO_2 injection and storage.

1. J. El-Ali, P. K. Sorger and K. F. Jensen, *Nature*, 2006, 442, 403-411.
2. R. L. Hartman and K. F. Jensen, *Lab Chip*, 2009, 9, 2495-2507.
3. S. Marre and K. F. Jensen, *Chem Soc Rev*, 2010, 39, 1183-1202.
4. P. Yager, T. Edwards, E. Fu, K. Helton, K. Nelson, M. R. Tam and B. H. Weigl, *Nature*, 2006, 442, 412-418.
5. F. Destremaut, J. B. Salmon, L. Qi and J. P. Chapel, *Lab Chip*, 2009, 9, 3289-3296.
6. Y. I. Yang, E. Jeong, I. Choi, S. Lee, H. D. Song, K. Kim, Y. Choi, T. Kang and J. Yi, *Angew Chem Int Edit*, 2011, 50, 4633-4636.
7. N. Liu, C. Aymonier, C. Lecoutre, Y. Garrabos and S. Marre, *Chem Phys Lett*, 2012, 551, 139-143.
8. A. M. Nightingale, S. H. Krishnadasan, D. Berhanu, X. Niu, C. Drury, R. McIntyre, E. Valsami-Jones and J. C. deMello, *Lab Chip*, 2011, 11, 1221-1227.

9. K. N. Toft, B. Vestergaard, S. S. Nielsen, D. Snakenborg, M. G. Jeppesen, J. K. Jacobsen, L. Arleth and J. P. Kutter, *Anal Chem*, 2008, 80, 3648-3654.
10. T. Pfohl, A. Otten, S. Koster, R. Dootz, B. Struth and H. M. Evans, *Biomacromolecules*, 2007, 8, 2167-2172.
11. M. E. Brennich, J. F. Nolting, C. Dammann, B. Noding, S. Bauch, H. Herrmann, T. Pfohl and S. Koster, *Lab Chip*, 2011, 11, 708-716.
12. K. Dhouib, C. K. Malek, W. Pfleging, B. Gauthier-Manuel, R. Duffait, G. Thuillier, R. Ferrigno, L. Jacquamet, J. Ohana, J. L. Ferrer, A. Theobald-Dietrich, R. Giege, B. Lorber and C. Sauter, *Lab Chip*, 2009, 9, 1412-1421.
13. R. Stehle, G. Goerigk, D. Wallacher, M. Ballauff and S. Seiffert, *Lab Chip*, 2013, 13, 1529-1537.
14. J. Becker, M. Bremholm, C. Tyrsted, B. Pauw, K. M. O. Jensen, J. Eltzholt, M. Christensen and B. B. Iversen, *J Appl Crystallogr*, 2010, 43, 729-736.
15. J. Bolze, D. Pontoni, M. Ballauff, T. Narayanan and H. Colfen, *J Colloid Interf Sci*, 2004, 277, 84-94.
16. G. Philippot, K. M. O. Jensen, M. Christensen, C. Elissalde, M. Maglione, B. B. Iversen and C. Aymonier, *J Supercrit Fluid*, 2014, 87, 111-117.
17. S. Marre, A. Adamo, S. Basak, C. Aymonier and K. F. Jensen, *Ind Eng Chem Res*, 2010, 49, 11310-11320.
18. S. Marre, Y. Roig and C. Aymonier, *J Supercrit Fluid*, 2012, 66, 251-264.
19. A. J. deMello, *Nature*, 2006, 442, 394-402.
20. B. Pinho, S. Girardon, F. Bazer-Bachi, G. Bergeot, S. Marre and C. Aymonier, *Lab Chip*, 2014, 14, 3843-3849.
21. K. F. Jensen, *Mrs Bull*, 2006, 31, 101-107.
22. S. Marre, J. Park, J. Rempel, J. Guan, M. G. Bawendi and K. F. Jensen, *Adv Mater*, 2008, 20, 4830-+.
23. R. Couto, S. Chambon, C. Aymonier, E. Mignard, B. Pavageau, A. Erriguible and S. Marre, *Chem Commun*, 2015, 51, 1008-1011.
24. R. L. Hartman, J. P. McMullen and K. F. Jensen, *Angew Chem Int Edit*, 2011, 50, 7502-7519.
25. K. F. Jensen, B. J. Reizman and S. G. Newman, *Lab Chip*, 2014, 14, 3206-3212.
26. B. E. Warren, *J Am Ceram Soc*, 1992, 75, 5-10.
27. T. Beuvier, B. Calvignac, G. E. J. R. Delcroix, M. K. Tran, S. Kodjikian, N. Delorme, J. F. Bardeau, A. Gibaud and F. Boury, *J Mater Chem*, 2011, 21, 9757-9761.
28. E. A. C. Panduro, T. Beuvier, M. F. Martinez, L. Hassani, B. Calvignac, F. Boury and A. Gibaud, *J Appl Crystallogr*, 2012, 45, 881-889.
29. C. Carteret, A. Dandeu, S. Moussaoui, H. Muhr, B. Humbert and E. Plasari, *Cryst Growth Des*, 2009, 9, 807-812.
30. D. C. Popescu, M. M. J. Smulders, B. P. Pichon, N. Chebotareva, S. Y. Kwak, O. L. J. van Asselen, R. P. Sijbesma, E. DiMasi and N. A. J. M. Sommerdijk, *J Am Chem Soc*, 2007, 129, 14058-14067.
31. L. Brečević and A. E. Nielsen, *Journal of Crystal Growth*, 1989, 98, 504-510.
32. L. N. Plummer and E. Busenberg, *Geochimica et Cosmochimica Acta*, 1982, 46, 1011-1040.
33. H. B. Yin, B. Z. Ji, P. S. Dobson, K. Mosbahi, A. Glidle, N. Gadegaard, A. Freer, J. M. Cooper and M. Cusack, *Anal Chem*, 2009, 81, 473-478.
34. A. Yashina, F. Meldrum and A. deMello, *Biomicrofluidics*, 2012, 6.
35. C. Y. Zhang, K. Dehoff, N. Hess, M. Oostrom, T. W. Wietsma, A. J. Valocchi, B. W. Fouke and C. J. Werth, *Environ Sci Technol*, 2010, 44, 7833-7838.
36. B. L. Henke, E. M. Gullikson and J. C. Davis, *Atom Data Nucl Data*, 1993, 54, 181-342.